DALM, Deformable Attenuation-Labeled Mesh for Tomographic Reconstruction and Segmentation

Jakeoung Koo, Anders Bjorholm Dahl, and Vedrana Anderson Dahl

***Abstract*—Most X-ray tomographic reconstruction methods represent a solution as an image on a regular grid. Such representation may be inefficient for reconstructing homogeneous objects from noisy or incomplete projections. Here, we propose a mesh-based method for reconstruction and segmentation of homogeneous objects directly from sinogram data. The outcome of our proposed method consists of curves outlining the regions of constant attenuation, and this output is represented using a labeled irregular triangle mesh. We find the solution by deforming the mesh to minimize the residual given by the sinogram data. Our method supports multiple materials, and allows for topological changes during deformation. An integral part of our algorithm is an efficient forward projection of the labeled mesh onto the sinogram domain. We initialize our algorithm based on graph total variation, also here taking advantage of the mesh representation. Experimental results on simulated datasets show that our method gives a compact representation of the reconstruction and also accurate segmentation results for challenging data with e.g. large noise, a small number of angles or problems with limited angle. We also demonstrate the result on real fan-beam data. The proposed geometric solution shows a further step towards using alternative representations for tomographic reconstruction.**

***Index Terms*—Deformable models, tomographic reconstruction, tomographic segmentation.**

I. Introduction

In X-RAY CT, the aim of the tomographic reconstruction is typically to compute an image of a scanned object with image voxels representing attenuation coefficients arranged on a regular grid [1]. This representation is well-suited for a wide range of reconstruction problems. However, for homogeneous objects with simple geometry, grid-based representation may be very redundant.

In this work, we propose a reconstruction and segmentation method using an interface-based representation in the form of a labeled deformable mesh and we investigate the properties of our method. The proposed method is targeted at objects composed of homogeneous components. Our work extends the method by Dahl *et al.* [2] that employs a deformable closed curve to outline one object in the reconstruction. Here, we replace one single curve by an interface represented as edges in a labeled mesh, and we deform the interface based on Deformable Simplicial Complex (DSC) proposed by Misztal and Bærentzen [3]. This gives our method several advantages compared to [2]. First, we can reconstruct multiple objects thanks to topological adaptivity of DSC. Second, as DSC supports multi-label segmentation, our method also supports objects with different materials. Third, DSC may employ either fixed or adaptive mesh resolution, which gives an additional flexibility to our method. Fourth, while in [2] an initialization is done by circle, meshing of the reconstruction domain allows us to efficiently initialize our algorithm by finding a configuration close to the desired solution.

In Fig. 1 we show an example of a labeled mesh before and after the deformation. To obtain a segmentation, we compute the

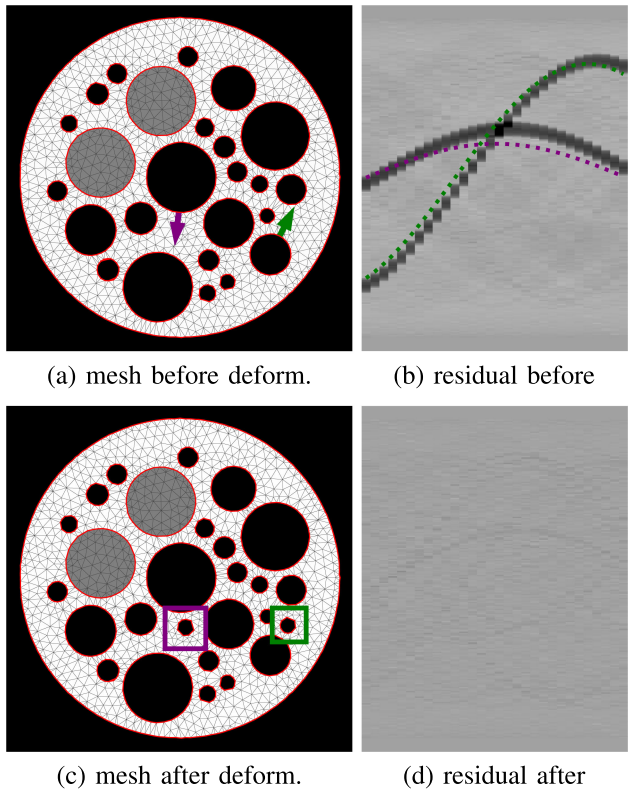

(a) mesh before deform. (b) residual before

(c) mesh after deform. (d) residual after

Fig. 1. Mesh deformation minimizes the residual. A mesh configuration (a) with triangle labels indicated by colors (black, gray and white) and interface drawn in red. This configuration yields a residual (b) where the dark regions denote large values. Two large displacements in the normal direction are shown as the arrows in (a) and their corresponding residuals are shown as dotted lines in (b). After deformation, we obtain the mesh with two new regions (c) shown in rectangles, with the residual (d).

Manuscript received July 2, 2020; revised October 31, 2020 and January 8, 2021; accepted January 9, 2021. Date of publication January 15, 2021; date of current version February 8, 2021. This work was supported by the European Union's Horizon 2020 Research and Innovation Programme under the Marie Skłodowska-Curie Grant Agreement 765604. *(Corresponding author: Jakeoung Koo.)*

The authors are with the Department of Applied Mathematics and Computer Science, Technical University of Denmark, 2800 Lyngby, Denmark (e-mail: jakoo@dtu.dk; abda@dtu.dk; vand@dtu.dk).

Digital Object Identifier 10.1109/TCI.2021.3052034

displacements of the interface vertices to minimize the residual between data and the computed sinogram from the mesh. While moving those vertices, the mesh quality is maintained by splitting or merging nearby faces. These local mesh operations allow two new pores to be created from nearby pores.

A. Related Works

Two approaches to finding segmentations directly from sinogram data are related to our work: *discrete-valued tomography* and *deformable models*. We will review those two approaches in addition to *mesh-based reconstruction methods*.

Discrete-valued tomography methods assume that the reconstruction image has a small number of discrete attenuation coefficients. This acts as a prior to deal with situations where there are a small number of homogeneous objects from small angular range and noisy sinogram data. Batenburg and Sijbers in [4] proposed the DART method, which combines an existing iterative reconstruction method and a thresholding scheme. To improve DART's robustness to noise and to automatically compute the attenuation coefficients, extensions have been suggested in [5], [6], and [7].

The method in [8] splitted the variables representing attenuation coefficients into continuous and discrete. This splitting turns the problem into two simple problems solved by the conjugate gradient method and a submodular minimization solver. In [9] the authors suggested a joint reconstruction and segmentation method in a variational framework. Other techniques include graph cut [10], [11] and convex relaxation techniques [12]. These discrete-valued tomography methods relied on a regular image grid, while DALM does not restrict the solution on the image domain. Among these works, we choose one of the state-of-the-art works [7] to compare our segmentation results with.

Deformable models from sinogram data have been studied mostly based on level set methods [13]. Whitaker and Elangovan [14] formulated the Mumford-Shah piecewise constant model [15] in terms of level-set to minimize the reprojection error. This work was extended to a piecewise smooth model by Alvino and Yezzi [16]. Extending two-phase segmentation, a multi-phase piecewise constant model was studied in [17], [18]. The stated deformable models required dense and regular discretization. To reduce the unknown variables, a parametric level set method was proposed in [19] and used in [20]. Those methods required fewer parameters to represent a level set, which reduced the unknown variables and allows to use efficient second-order optimization methods.

Such level-set models rely on regular image grids and their forward projections use an image-based forward model, whereas the proposed method can directly project a labeled mesh into sinogram domain. Instead of level-set, our previous work [2] used an explicit representation, but limited to one simple closed object. We extend it to consider multiple materials and allow topological changes.

Several *mesh-based reconstruction methods* have been proposed. Such methods aim to find an adaptive representation of objects to match with the structure of objects and improve the reconstruction quality. In [21] Brankov *et al.* suggested a method to estimate an initial mesh configuration from the reconstruction image obtained by pixel-based filtered backprojection. This dependency on an analytical method could affect the mesh estimation step severely in the case of limited sinogram data. Cazasnoves *et al.* [22] employed a more sophisticated strategy to build an irregular mesh before reconstruction. They detected edges in sinogram data to extract structures in 2D and merge them to estimate the interface of objects in 3D. Around the interface, a more fine mesh was constructed and then the reconstruction was performed. Instead of estimating mesh configuration once, adaptive mesh refinement methods have been proposed. In [23], [24], a tetrahedron mesh was generated from a coarse regular grid and the Expectation Maximization (EM) method was used for reconstruction on the mesh. The mesh was finely refined around the nodes having large attenuation value variations. They repeated reconstruction and refinement in a coarse-to-fine way. On the other hand, the method in [25] began with a fine uniform grid and alternately use EM and coarsen the mesh, repeatedly. In [26] they iteratively refined the mesh based on the segmentation result by the level set method.

Unlike existing mesh-based reconstruction methods, our method aims to deform the interface between materials and uses the mesh as an auxiliary structure due to the assumption of a small number of materials.

B. Summary of Contributions and Outline

The main contribution of our work is to develop a mesh-based deformable method from sinogram data which supports multiple materials and topological changes during deformation (Sec. III). We develop an efficient forward projection algorithm mapping a labeled mesh into the sinogram domain. To avoid local optima, we employ a robust initialization scheme based on graph total variation on the mesh (Sec. IV). The numerical results are presented in noisy and incomplete synthetic data and in real fan-beam data (Sec. VI).

II. Problem Formulation

In this section, we formulate the tomographic segmentation problem to estimate the curves to segment the regions whose attenuation values are approximately homogeneous. We follow the similar formulation in [14], [16] which consider two-region segmentation, but we extend it to multi-region cases inspired by the region competition method [27]. Similar to such works, our formulation is based on variational methods where an energy over a continuous space is formulated and a low energy reflects a desired solution. Here, our aim is to find the minimizer. In the next section, we will propose a concrete algorithm to minimize the energy.

The sinogram data $p(\theta, s)$ is produced by projecting and rotating an unknown collection of objects onto the detector, and by θ we denote the projection angle, while s denotes the detector position.

Tomographic segmentation problem for homogeneous objects is to divide the reconstruction domain $\Omega \subset \mathbb{R}^2$ into M mutually disjoint regions $\{R_m\}$ such that $\Omega = \cup_{m=1}^{M} R_m$ and $R_i \cap R_j \neq \emptyset$ for $i \neq j$. Each region is associated to a homogeneous object with attenuation coefficient μ_m. We aim to find the curves $\{C_m\}$ to align with the boundaries of unknown objects such that $C_m = \partial R_m$ for each region R_m.

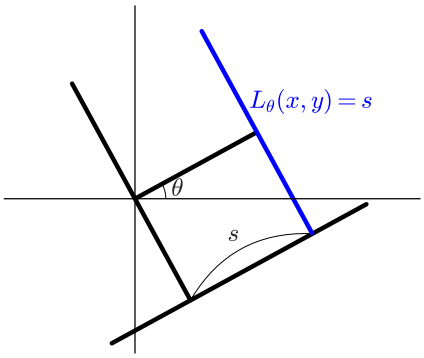

Fig. 2. Illustration of line equations for parallel beam. Given a position s along the detector, blue line represents the line equation $L_\theta(x,y)-s=0$.

From this configuration, we define $\mu_m\hat{p}_m$ as forward projection of a region R_m with the attenuation value μ_m where

$$\hat{p}_m(\theta,s)=\int_{R_m}\delta(L_\theta(x,y)-s)\,\mathrm{d}x\,\mathrm{d}y, \tag{1}$$

and δ is the delta function, s the detector position, θ the projection angle and $L_\theta-s=0$ a line ray equation. For the parallel beam, L is given by $L_\theta(x,y)=x\cos\theta+y\sin\theta$ (See Fig. 2). By combining all M materials, we define $\hat{p}$ as a linear combination of all the contributions

$$\hat{p}(\theta,s)=\sum_{m=1}^{M}\mu_m\hat{p}_m(\theta,s). \tag{2}$$

From the estimation $\hat{p}$, we aim to fit it to the sinogram data p, by minimizing the reprojection error $(p-\hat{p})^2$. This fitting term can lead to an undesirable solution if data is noisy or incomplete. To prevent it, we introduce a regularization term to make the curves smooth by penalizing their large lengths. With this smoothness term, we define the energy to minimize:

$$E(\{\mu_m,C_m\})=\frac{1}{2}\sum_{\theta,s}(p(\theta,s)-\hat{p}(\theta,s))^2+\lambda\sum_{m=1}^{M}\mathrm{Len}(C_m), \tag{3}$$

where λ is the weighting parameter for the regularization term and Len denotes the length of a closed curve, defined by $\mathrm{Len}(C_m)=\int_{C_m}\mathrm{d}r$, with arc length parameter r [28]. Choosing the optimal regularization parameter λ in (3) is not straightforward and other variational approaches [14], [16] have the same problem. We often have an idea of how object shapes look like before scanning. In this case, the prior knowledge on objects could help choose the parameter.

Given attenuation values $\{\mu_m\}$, we derive a curve evolution equation. Consider a curve C_m which encloses the region R_m with the attenuation μ_m and the adjacent region R_n with μ_n. Then, the curve evolution equation for C_m can be derived as (see Appendix)

$$C_m^{k+1}(r)=C_m^k(r)+\tau\left((\mu_m-\mu_n)\sum_{\theta}(p(\theta,\tilde{s})-\hat{p}(\theta,\tilde{s}))+\lambda\kappa_m(r)\right)N_m(r), \tag{4}$$

where k denotes the iteration number, τ the step size, N_m the outward normal vector, κ_m the curvature of the curve and $\tilde{s}=L_\theta(C_m(r))$ the detector positions onto which the point $C_m(r)$ are projected.

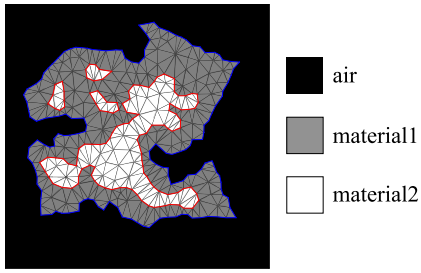

Fig. 3. Illustration of attenuation-labeled mesh. Each triangle is associated with one material. The blue edges indicate the interface between air and the material 1 and the red edges between the material 1 and the material 2. For the illustration, the triangles representing the background are omitted.

III. Deformable Attenuation-Labeled Mesh

In this section, we describe the proposed framework, deformable attenuation-labeled mesh (DALM), to optimize the energy in (3). We first propose our mesh-based representation, called ALM, and its forward projection to generate the estimated sinogram. From the estimation, we compute the attenuation values and deform ALM.

A. Attenuation-Labeled Mesh (ALM)

Consider a triangularization of a reconstruction domain $\Omega\subset\mathbb{R}^2$, where every triangle is labeled with a label m from $m\in\{1,\ldots,M\}$, and every label has an associated value μ_m. In terms of tomographic reconstruction, labels correspond to different materials, and label values correspond to material attenuations. While we can operate with an arbitrary number of materials, we assume that M is known as a prior and much smaller than the number of triangles.

The construction consisting of a triangle mesh, labels, and attenuation values is denoted by $\mathcal{X}$, and we call it *attenuation-labeled mesh (ALM)*. Any ALM configuration is fully defined by the list of mesh vertices, list of mesh triangles, list of triangle labels, and a list of label attenuations. An example of ALM is illustrated in Fig. 3.

Clearly, ALM gives a partitioning of the reconstruction domain Ω into different materials, i.e. regions R_m of attenuation μ_m, for $m=1,\ldots,M$. Furthermore, ALM gives an explicit representation of interface curves as a collection of *interface edges* – mesh edges whose two adjacent triangles are assigned two different labels. Furthermore, we define *interface vertices* as mesh vertices which are adjacent to at least one interface edge.

B. Forward Projection of ALM

We propose a forward projection algorithm to yield the estimated sinogram $\hat{p}$ from the interface edges of a configuration of ALM. Our forward model is based on the principle that a ray should hit a closed region an even number of times. Our forward algorithm has two advantages: First, we only need the information of the interface and its surrounding labels. Second, the forward projection can be done independently for each interface edge, which allows for efficient parallelization.

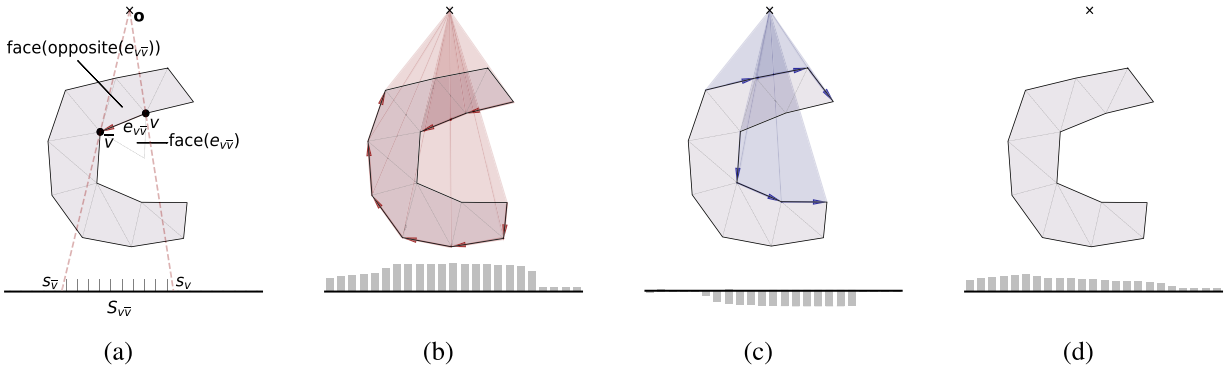

Fig. 4. Illustration of mesh representation and forward projection in fan-beam geometry for a projection angle. For the illustration purpose, we omit the triangles representing background and the interface edges are shown as darker than non-interface edges. (a) Half-edge based mesh is used to represent objects where each face is labeled with a material. The shaded region denotes a material and its outside denotes vacuum. The detector positions $s_v, s_{\bar{v}}$ are from the two vertices in a half-edge. Depending on the sign of $(s_v - s_{\bar{v}})$, we add (b) or subtract (c) the contribution of the segment between the source and the interface. After summing these values, we obtain (d) the final forward projection for a specific angle.

Algorithm 1: Forward Projection For One Angle.

Input: Attenuation-labeled mesh $\mathcal{X}$, a projection angle θ
Init: $\hat{p}_m(\theta, s) \leftarrow 0$ for every label m, detector pixel s
for all interface edge e_{ij} **do**
  $l \leftarrow$ label of triangle left of e_{ij}
  $k \leftarrow$ label of triangle left of e_{ji} (opposite triangle)
  $s_i \leftarrow$ projection of i onto the detector (continuous)
  $s_j \leftarrow$ projection of j onto the detector (continuous)
  for all detector pixel s between s_i and s_j **do**
    $o \leftarrow$ source position
    $x \leftarrow$ intersection of e_{ij} and ray $\overline{os}$
    $c \leftarrow$ length of $\overline{ox}$
    $\hat{p}_l(\theta, s) \leftarrow \hat{p}_l(\theta, s) + \text{sign}(s_i - s_j) \cdot c$
    $\hat{p}_k(\theta, s) \leftarrow \hat{p}_k(\theta, s) + \text{sign}(s_j - s_i) \cdot c$
  end for
end for
return $\hat{p}(\theta, s) \leftarrow \sum_{m=1}^{M} \mu_m \hat{p}_m(\theta, s)$

In Fig. 4, we provide an illustration of our forward algorithm for fan-beam geometry given one projection angle. We (b) add or (c) subtract the contribution between the source point and the interface, depending on the orientation of the half-edges. The sign of the contribution is determined by the sign of the difference of detector positions $s_v, s_{\bar{v}}$ corresponding to the initial and end vertices $v, \bar{v}$ in the edge, respectively. Then, we (d) sum those signed contributions. The whole procedure for one projection angle is summarized in Algorithm 1. After performing forward projection for all edges and angles, we obtain the final estimated sinogram.

C. Estimation of Attenuations

In the energy (3), we have two unknowns of attenuation values and interface curves. Our strategy is to optimize them separately. Here, we fix the interface curves and optimize M attenuation values only. The optimal condition with respect to μ_m reads

$$0 = \frac{\partial E}{\partial \mu_m} = -\sum_{\theta,s} (p(\theta, s) - \hat{p}(\theta, s)) \hat{p}_m(\theta, s), \qquad (5)$$

which leads to a system of linear equations to solve:

$$\begin{pmatrix} \sum_{\theta,s} \hat{p}_1^2 & \cdots & \sum_{\theta,s} \hat{p}_1 \hat{p}_M \\ \vdots & \ddots & \\ \sum_{\theta,s} \hat{p}_M \hat{p}_1 & & \sum_{\theta,s} \hat{p}_M^2 \end{pmatrix} \begin{pmatrix} \mu_1 \\ \vdots \\ \mu_M \end{pmatrix} = \begin{pmatrix} \sum_{\theta,s} \hat{p}_1 p \\ \vdots \\ \sum_{\theta,s} \hat{p}_M p \end{pmatrix}, \qquad (6)$$

where we omit (θ, s) in $\hat{p}_m$, p for simplicity of notation. The matrix on the left side is symmetric and positive semi-definite. In many cases, the background of a material is known as air or vacuum, so its attenuation coefficient can be set as zero. In this case, we only need to estimate $M - 1$ attenuation coefficients. If the number of unknown attenuation coefficients in (6) is less than 4, we can use the closed-form solution to compute the inverse of the matrix of size 2-by-2 or 3-by-3 in the left hand side. Otherwise, we can use Cholesky factorization [29] to solve (6).

D. Deformation of ALM

Given attenuation values, we now deform the interface in the direction of minimizing the energy (3). In ALM, each vertex v on the interface is associated with two materials: the inside μ_v and the outside $\tilde{\mu}_v$. For example, μ_v corresponds to the material for the triangle: `face(opposite(`$e_{v\bar{v}}$`))` in Fig. 4(a). For each interface vertex v, we compute the displacement from the current position, by the discretization of (4), as follows:

$$\tau \left((\mu_v - \tilde{\mu}_v) \sum_{\theta} (p(\theta, s_v) - \hat{p}(\theta, s_v)) + \lambda \kappa_v \right) N_v, \qquad (7)$$

where N_v denotes the outward unit normal vector for the vertex v and κ_v is the curvature for the vertex v which can be computed by the discrete version of Frenet formula [28]. The detector position s_v denotes the position determined by the vertex v and projection geometry, as shown in Fig. 4(a). Note that s_v needs to be interpolated, as detectors have finite measurements.

From the computed displacements, we aim to deform the interface. To allow for topological changes during evolution, we employ a mesh-based deformable model, Deformable Simplicial Complex (DSC) [3]. Here we briefly explain the principle of DSC.

DSC moves the interface vertices sequentially towards destinations, while improving the mesh quality. The improvement

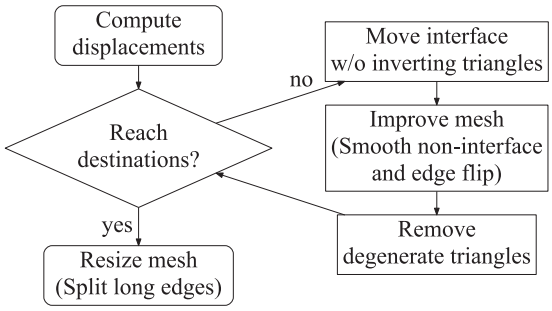

Fig. 5. A diagram of the deformation step in DSC. The loop is done for one vertex at a time. After all the vertices reach the destination, the mesh is resized.

step includes smoothing non-interface vertices, edge flipping and removing degenerate faces. The destination of each interface vertex is computed from (7) which is the displacement from the current position. When all the interface vertices reach their destinations, DSC refines the mesh further by splitting long edges, which are not on the interface, based on the parameter of average edge length l_1. This parameter allows some range of edge lengths around l_1. At this last step, DSC does not split the interface edges.

We provide a summary of DSC deformation in Fig. 5. We refer to the paper [3] for more detailed description of DSC.

IV. Initialization

Snake-based reconstruction suggested in [2] is initialized as a circle in the middle of the reconstruction domain. Such initialization would also work in our case, and topological adaptivity provided by DSC would split the curve if needed. Despite the topological adaptivity, the curve deformation might still stop in a local optimum, for example if a hole needs to be introduced in the material.

To avoid local optima, and to improve the efficiency of the reconstruction, it is desirable to start the mesh deformation from a good initialization. We present two initialization methods, the first based on filtered backprojection and the second based on a graph total variation. The first method is computationally efficient and aimed for complete and noise-free data. The second method is capable of handling incomplete or noisy data at an increased computational complexity.

Both initialization methods share a common pipeline. First, we construct a regular triangular mesh using a selected edge length l_0. Second, for each mesh triangle t we compute an attenuation coefficient ν_t. Third, we divide triangle attenuation coefficients into background and foreground objects by the k-means algorithm [30]. The difference between the two proposed initialization approaches lies in the second step, computing ν_t.

A. Filtered Backprojection on Mesh

Filtered backprojection method is one of the most popular methods in tomographic reconstruction [31]. This analytical method consists of two stages: filtering the sinogram and backprojection. Filtering sinogram does not depend on the representation of unknown objects, while the backprojection stage depends on the representation. In image reconstruction, for each pixel, the corresponding sinogram values are accumulated from all angles. Motivated by this way, we use a similar backprojection method on a triangular mesh.

For each mesh triangle t, we can compute its forward projection $\nu_t \hat{p}_t(\theta, s)$ with the attenuation ν_t by Algorithm 1. Then, the estimated sinogram corresponding to the whole mesh would be

$$\hat{p}_{\text{mesh}}(\theta, s) = \sum_{t=1}^{T} \nu_t \hat{p}_t(\theta, s)\,, \tag{8}$$

where T is the number of triangles in the mesh. This can be written as a matrix-vector product

$$\hat{p}_{\text{mesh}} = A\nu\,, \tag{9}$$

where $\hat{p}_{\text{mesh}}$ is unwrapped into a vector, A is the forward matrix whose t-th column is (unwrapped) $\hat{p}_t$ and ν is the unknown vector whose t-th element is ν_t.

From this setting, the backprojection operator is the adjoint operator of A, and the backprojected image is

$$\nu_{\text{B}} = A^T p. \tag{10}$$

Similar to filtered backprojection on images, we first filter the sinogram and backproject it onto the mesh as in (10).

B. Graph Total Variation

The filtered backprojection method is vulnerable to incomplete or noisy data. To deal with degraded data, we present another initialization method based on graph total variation [32]. In the mesh domain, we impose smoothness between the neighboring faces.

To formulate a minimization problem, we consider the absolute difference of attenuation coefficients of neighboring faces

$$E_{\text{smooth}} = \alpha \sum_{(t,\bar{t})\in\mathcal{E}} |\nu_t - \nu_{\bar{t}}|, \tag{11}$$

where $\mathcal{E} = \{(t, \bar{t}) : \text{trianges } t \text{ and } \bar{t} \text{ are adjacent}\}$ denotes a set of edges connecting two neighboring faces and α is a smoothness weight. This term can be written in a matrix multiplication form as

$$E_{\text{smooth}} = \|K\nu\|_1\,. \tag{12}$$

Here, K is an oriented edge-triangle incidence matrix with weight α. Each row of K represents one edge $(t, \bar{t})$, and has two non-zero elements: α in a position corresponding to triangle t and $-\alpha$ in a position corresponding to triangle $\bar{t}$.

Combining a data fidelity term of reprojection error and smoothness term (12), we aim at finding ν by solving the following minimization problem:

$$\nu_{\text{TV}} = \arg\min_{\nu} \frac{1}{2}\|A\nu - p\|_2^2 + \|K\nu\|_1. \tag{13}$$

Note that the weighting parameter α is incorporated into the matrix K.

Optimizing the convex energy (13) is not straightforward, as the energy has a non-smooth regularization term and two linear operators of A and K in the composite form. To deal with these difficulties, we employ the Hybrid Gradient Primal Dual (HGPD) algorithm [33] which can split the operators and lead to efficient iteration steps. To split the linear operators, we introduce two variables $z_1 = A\nu$, $z_2 = K\nu$ and the corresponding dual variables q_1, q_2. We also impose the positivity constraint

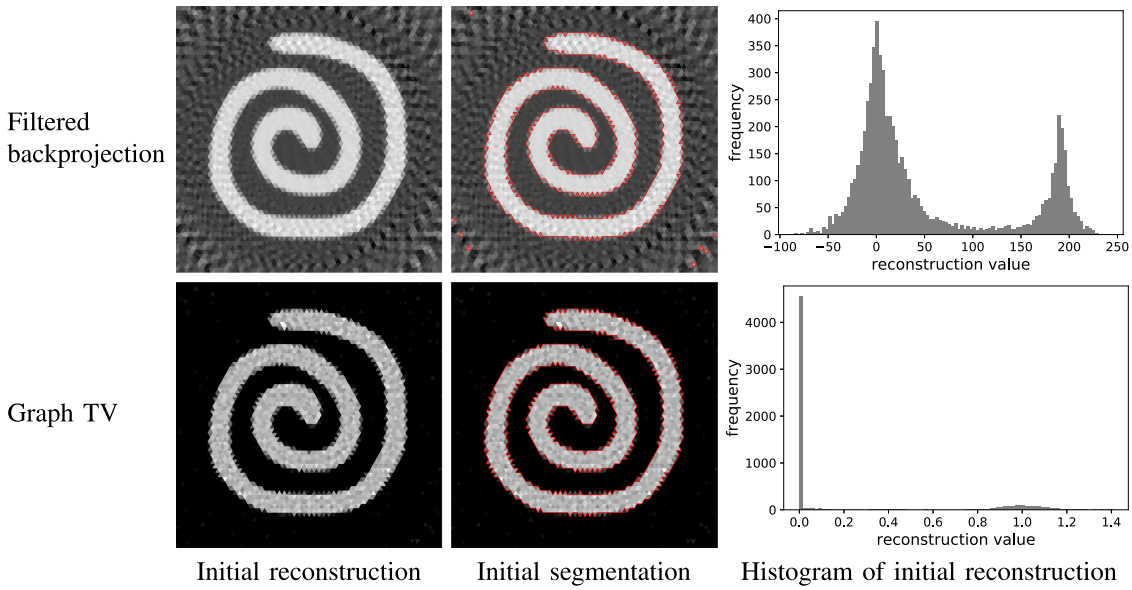

Fig. 6. An illustration of initialization schemes. In initial reconstructions, each triangle has its own attenuation value. In initial segmentation, the red line represents the initial guess of the object after applying k-means algorithm to initial reconstruction.

on our solution ν. To use HGPD, we formulate a saddle-point problem

$$\min_{\nu} \max_{q_1,q_2} \langle A\nu, q_1\rangle + \langle K\nu, q_2\rangle + \delta_+(\nu) - F^*(q_1, q_2), \quad (14)$$

where δ_+ is the indicator function of positive set and F^* is the conjugate function of $F(z_1, z_2) = \frac{1}{2}\|z_1 - p\|_2^2 + \|z_2\|_1$.

HGPD aims to find a saddle point solution of (14) by the minimization with respect to the primal variables and the maximization with respect to dual variables. The updates of primal and dual variables are provided in Algorithm 2. For the detailed derivation we refer to [34, Algorithm 4].

Algorithm 2: Primal Dual Updates For Solving (13).

Set the step sizes τ, σ as $1/(\|A\|_2 + \|K\|_2)$.
Initialize ν^0, q_1^0, q_2^0 as zero vectors.
for $k = 0, 1, 2, \ldots$

$$\nu^{k+1/2} := \nu^k - \tau(A^T q_1^k + K^T q_2^k) \quad (15)$$

$$\nu^{k+1} := \max(\nu^{k+1/2}, 0) \quad (16)$$

$$\bar{\nu} := 2\nu^{k+1} - \nu^k \quad (17)$$

$$q_1^{k+1} := \frac{q_1^k + \sigma(A\bar{\nu} - b)}{1+\sigma} \quad (18)$$

$$q_2^{k+1} := \frac{q_2^k + \sigma K\bar{\nu}}{\max(1, |q_2^k + \sigma K\bar{\nu}|)} \quad (19)$$

Fig. 6 shows an illustration of two different methods. We use the same phantom and sinogram data with 30 angles. For filtered backprojection, we use Hann filter. The reconstruction from filtered backprojection has some unstable values around the boundary, which gives several outliers in the initial segmentation. On the other hand, graph total variation yields a better result with clean background due to the local smoothness and positivity constraint.

Algorithm 3: DALM.

Input: sinogram data p, number of materials M
Output: attenuation-labeled mesh $\mathcal{X}$
1: Construct an initial mesh with regular edge length l_0
2: Compute initial reconstruction ν by Algorithm 2
3: Construct an initial ALM $\mathcal{X}$ by applying k-means to ν
4: **while** stop condition not met**do**
5: Forward projection of ALM by Algorithm 1
6: Estimate attenuations by (6)
7: Estimate displacements by (4)
8: Deform the ALM $\mathcal{X}$ by DSC
9: **end while**

V. Combined Method

Combining the initialization scheme, we summarize our proposed method, DALM, in Algorithm 3. We estimate an initial configuration by reconstructing attenuations on regular mesh and clustering them by k-means method [30]. This clustering yields an initial attenuation-labeled mesh (ALM). We iteratively update attenuation coefficients and deform ALM. This procedure repeats until the magnitude of deformation is less than a threshold or the iteration number exceeds 500.

VI. Experimental Results

In this section, we perform experiments to demonstrate the robustness and the limitation of DALM. We illustrate the adaptivity of topological changes and investigate the initialization methods. We show the relative advantages over other reconstruction methods on various synthetic datasets. We also investigate the

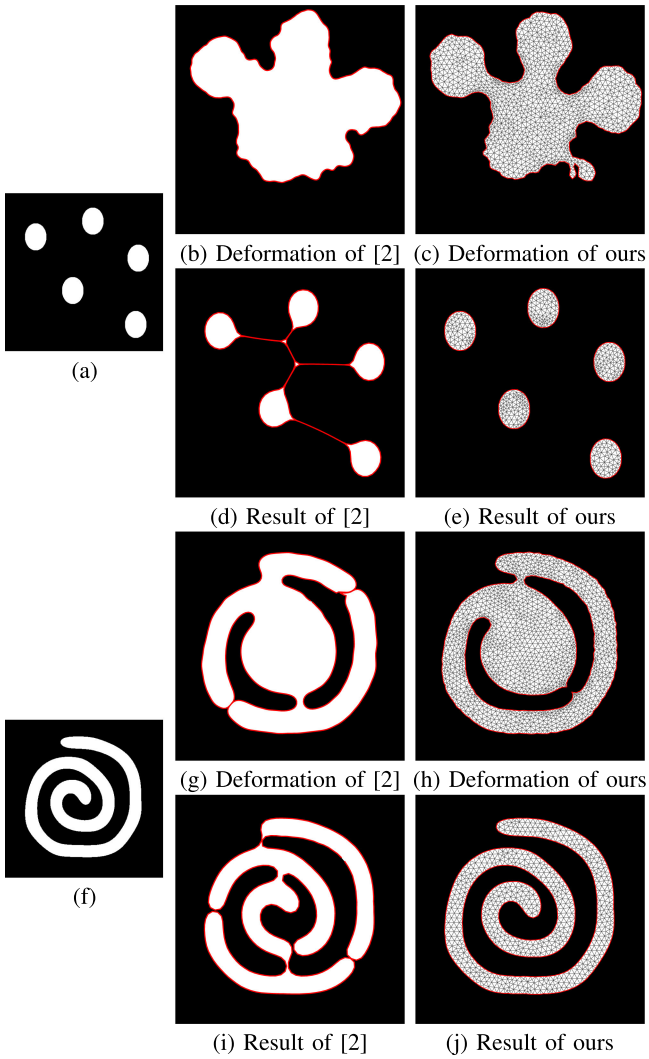

Fig. 7. DALM supports topological changes and captures complex shapes. The first column shows two phantom objects to be reconstructed. The second column shows the intermediate step and the final result of [2] from the circle initialization, where (b) and (d) are from the data generated by (a) and (g) and (i) are by (f). The last column shows the corresponding results of DALM from the same initialization.

numerical performance and the effects of algorithm parameters. Finally, we present results on real fan-beam data.

A. Support of Topological Changes During Deformation

Here, we illustrate one advantage of our method: topological adaptivity during deformation. Fig. 7 shows behaviour of our method compared to [2] on the two phantoms (a) and (f). The sinogram data are generated from the phantoms with parallel beam geometry and 30 angles. To better illustrate the curve evolution, we initialize both methods as circles. For the phantom (a), as shown in (b) and (d), a single curve used in [2] does not allow for change in topology during the curve evolution. The curves of the proposed method are shown in (c) and (e). The curves (interfaces) are red edges between faces labeled as foreground (white) and background (black). While moving interface vertices, the mesh quality is maintained by splitting or merging nearby faces. These local mesh operations allow for topological changes of objects during deformation. Support for topological adaptivity also helps reconstructing the complex shape (f). As shown in (g) and (i), the deformation of [2] stops in a local minimum, whereas our method successfully recovers the spiral shape (j).

B. Choice of Initialization and Parameters

As explained in Sec. IV, graph total variation can provide a more robust initialization than filtered backprojection. To deal with incomplete data, we choose the graph total variation method as the initialization throughout the next experiments.

Unless explicitly mentioned, we choose algorithm parameters as follows. As for initialization, we fix the initial edge length l_0 as 4, the smoothness parameter α as 8 and iterate the primal dual updates in (2) up to 200 times. As for the deformation of mesh, we fix the average edge length l_1 as 4, λ as 0.01 and set the maximum iteration number as 500. The step size τ for the curve evolution is set as 0.2. We use the public code for DSC provided the authors [3] and use the default parameters.

C. Robustness to Limited Data

In this set of experiment, we aim to show the relative advantage over other reconstruction methods on limited dataset.

We use the synthetic phantom images shown in the second column of Fig. 8 where Phantom 3 is generated from [35]. Each phantom has a fixed number of materials. Note that our forward projection requires a geometric representation of objects, while algebraic reconstruction methods need a discrete image. To compare fairly and avoid inverse crime, we generate sinogram data from images with 512-by-512 size by forward projection provided in the ASTRA toolbox [36] onto the detector with 256 pixels. Note that we do not employ our forward model to generate data, but employ an image-based forward model. We use a parallel beam geometry and choose the area projection model, which determines the weight in a pixel by the intersection area of the pixel and the ray whose width is the same as that of one detector pixel.

We compare DALM to other reconstruction methods including (image-based) Filtered Back Projection (FBP), Simultaneous Algebraic Reconstruction Technique (SART) [37] and Total Variation Regularized Discrete Algebraic Reconstruction Technique (TVR-DART) [7]. TVR-DART is one of the state-of-the-art discrete tomography methods where reconstruction images are assumed to have a fixed number of attenuation coefficients. This method is closely related to ours, as it gives an already segmented reconstruction. We carefully choose the regularization parameter of TVR-DART for fair comparison. Since the test data is generated from the image, these image-based methods have benefits in the reconstruction. We use the implementation of these methods based on ASTRA toolbox [36]. Other lines of works are learning-based methods using deep neural networks when training data is available. Although such approaches obtain impressive performance in some cases, our method is aimed at another set of problems where no training data is needed. Hence, we compare against the mentioned model-based methods, rather than data-driven methods.

Small number of projections: We use sinogram data with a small number of angles between 0 and 180 degrees. In Fig. 8,

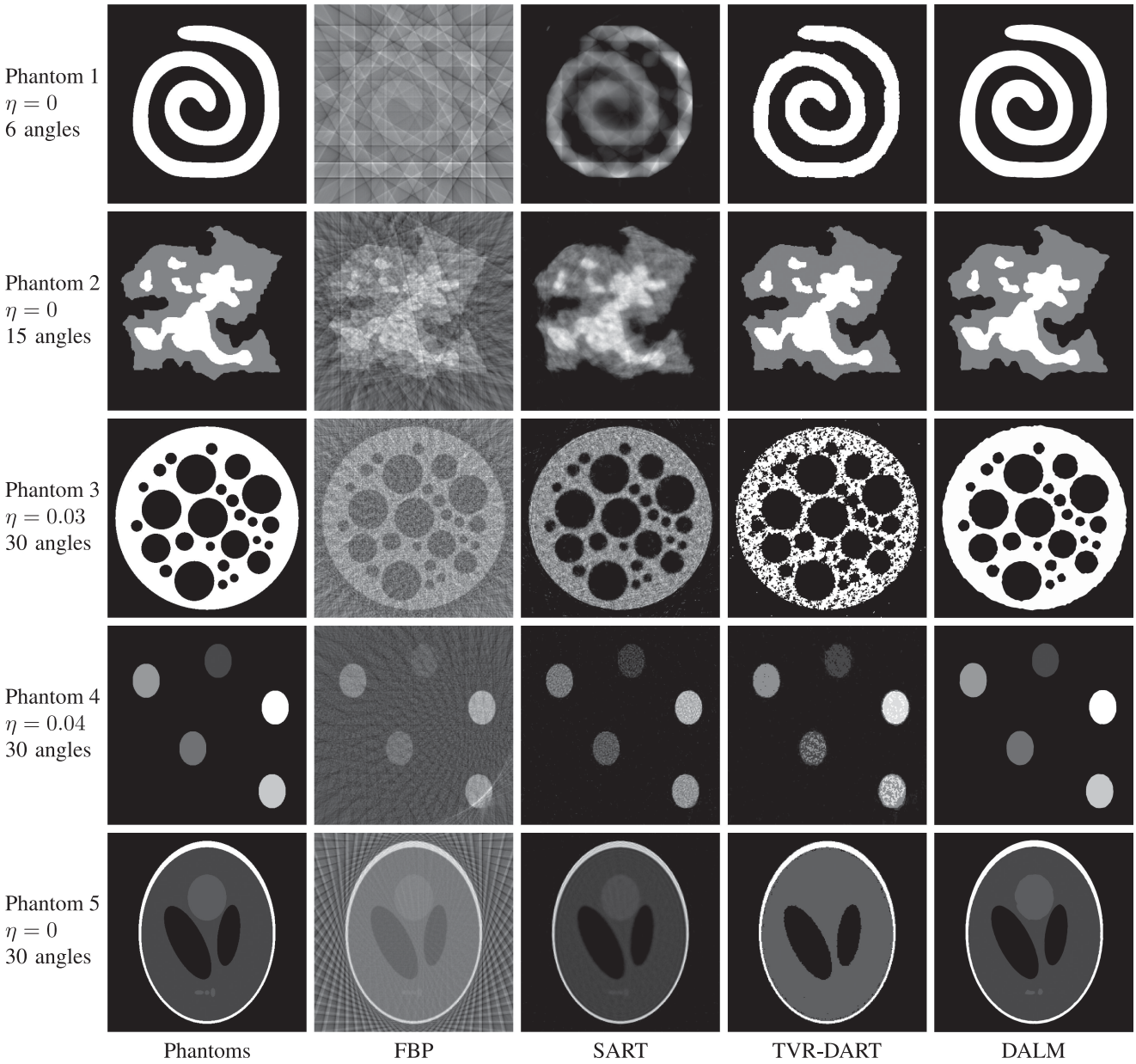

Fig. 8. Qualitative results on phantom data with small number of projections. Each row uses the different number of angles in sinogram data generated from the phantom images in the second column. The first column indicates the numbers of angles used and relative noise level η. The 3nd-5th columns show the reconstruction image by FBP, SART and TVR-DART, respectively. The last column shows our results based on geometric representation.

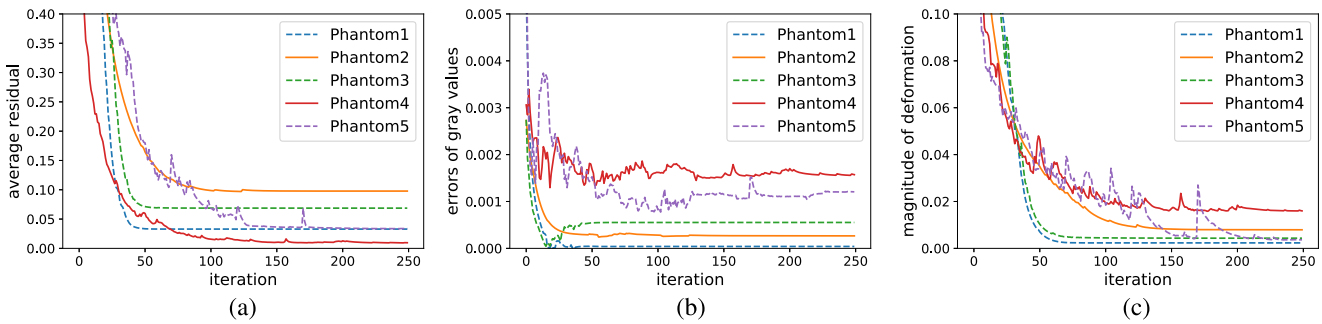

Fig. 9. Convergence behavior on phantom images in Fig. 8. (a) Convergence of residuals divided by the size of sinogram data. (b) Convergence of the gray value (attenuation coefficients) errors which are sum of absolute differences of true attenuation coefficients and estimations divided by the number of materials. (c) Convergence of the magnitude of deformation which is the mean value of displacements on the interface vertices.

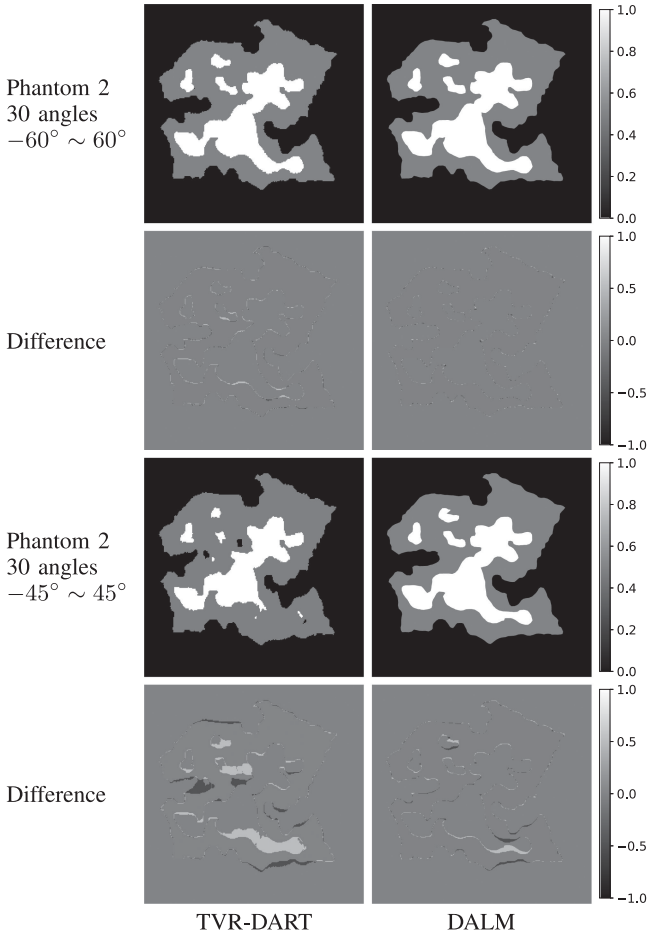

Fig. 10. Visual comparison of reconstruction results on limited angle data between TVR-DART and DALM. The odd rows show the reconstruction results and the even rows show the difference image to ground truth.

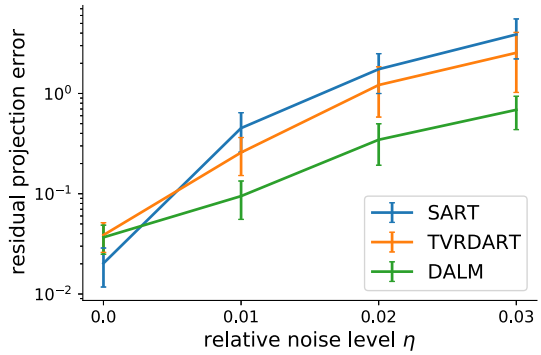

Fig. 11. Error measure with varying relative noise level for residual projection error between noise-free sinograms and estimations. The error bars show the mean and standard deviations of the errors with respect to 5 phantom data.

we present the qualitative results with different angles chosen to give reasonable results. In this figure, η denotes the relative Gaussian noise level. The details about imposing noise will be explained in VI-D. For Phantom 1 and Phantom 2, TVR-DART and our method are shown to give accurate reconstruction results even for a small number of angles. However, TVR-DART yields a degenerate reconstruction result for Phantom 3 due to high noisy levels, while DALM captures the overall shape of foams. TVR-DART also yields an inaccurate reconstruction in Phantom 4 which has 6 materials and in Phantom 5 which has 4 materials with small features. As indicated in its original paper, TVR-DART seems to be degenerate when the object have many materials. On the other hand, DALM overall captures the shapes in Phantom 4, but our method still misses one tiny feature at the right bottom part, as can be seen if we zoom in close enough. In Phantom 5, our method also has difficulty segmenting a fine detail on the bottom, but gives better result than TVR-DART.

Limited range of angles: In this experiment, we use Phantom 2, but generate sinogram with limited range of angles. In Fig. 10, we present the qualitative results from limited angle data. The first row shows the result from data with 30 limited angles between -60° to 60° and the second row shows the difference of the results to the ground truth. Both TVR-DART and our method yield good reconstruction shapes, but TVR-DART gives an inaccurate attenuation coefficient. The third row shows the visual results where a smaller range of angles (-45° to 45°) are used. The reconstruction by TVR-DART is inaccurate in shape and attenuation coefficient value. DALM gives a superior result to that of TVR-DART.

Convergence behavior: In Fig. 9, we investigate the convergence behavior of DALM for noise-free phantom data with uniformly-sampled 30 angles. In (a), we show the residual between the sinogram data and our estimated sinogram divided by the number of angles and detector pixels per iteration. The behaviors of phantoms 1, 2 and 3 show smooth curves, while the phantoms 4 and 5 have some peaks. This instability can arise when some regions are merged or splitted. In the end, the residual is shown to be stable. In (b) we plot the errors of attenuation coefficients per iteration which are measured as the sum of absolute differences between true attenuation coefficients and the estimates μ_m divided by the number of materials. As for Phantom 1 and 3, the gray value (attenuation coefficient) error is shown to increase around the 20th iteration. This happens because we estimate the optimal attenuation coefficients given the current mesh. Therefore, large changes in the mesh can affect the estimation of attenuation coefficients. In Phantom 4 and 5, the errors are shown to stablize after around 190 iterations. In (c) we show the magnitude of deformation per iteration which is calculated as the average of displacements on interface vertices. These displacements are calculated from the expression within the large parenthesis in (4). Because the step size is chosen around 0.2, the exact magnitude of deformation is smaller than those shown. Both errors of attenuation coefficients and magnitude of deformation begin to be stable in the end.

D. Robustness to Noise

In the following, we compare our method to other methods quantitatively with different noise levels. In this set of experiment, we use all the 5 phantoms and generate sinogram data with 30 projection angles. We impose Gaussian noise e on some sinogram data p such that a noisy sinogram is given as $\bar{p} = p + e$. The noise e is determined by varying the relative noise level $\eta = \|e\|_2/\|p\|_2$ from 0 to 0.03.

We employ a metric *residual projection error* [38] between the noise-free sinogram p and the estimated sinogram $\hat{p}$. This estimated sinogram $\hat{p}$ is obtained by forward projection of the

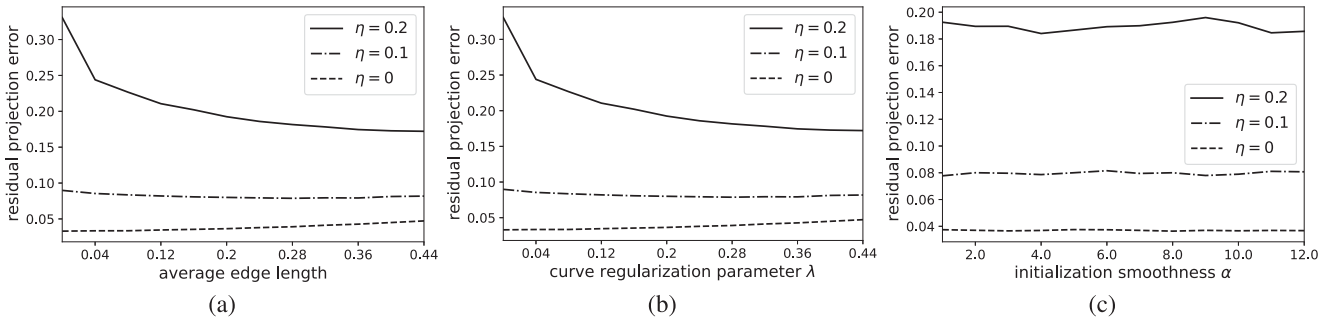

Fig. 12. Effect of algorithm parameters with different noise levels η in terms of residual projection error. Effect of (a) edge length parameter, (b) curve regularization parameter λ and (c) smoothness parameter α in the initialization. In (a) initial edge length l_0 and average edge length l_1 during deformation are set as the same values. Phantom 1 is used for this result.

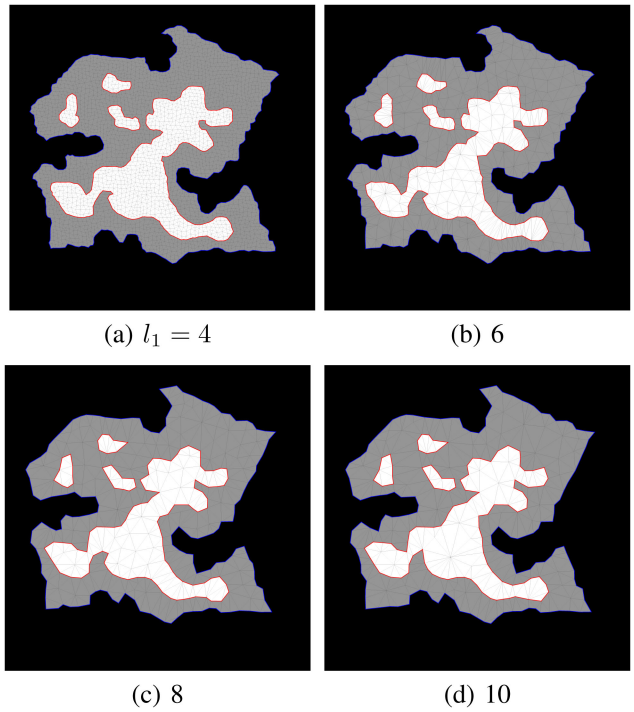

Fig. 13. Effect of average edge length l_1. Final mesh results of Phantom 3 are shown with varying average edge length, starting from the same initialization.

reconstruction. Then, the residual projection error is the mean squared error between between the noise-free sinogram p and the estimation $\hat{p}$.

In Fig. 11, we present residual projection errors with varying relative noise level η. When there is no noise, SART gives the best result as it aims to minimize the residual without regularization. However, as noise level increases, DALM is shown to yield better results than other methods.

In image-based reconstruction, it is common to evaluate the quality of reconstruction based on image quality metrics such as peak signal-to-noise ratio (PSNR) or structural similarity index (SSIM). To use such metrics, from our DALM solutions we produce images of size 256×256, the same size as reconstructions by image-based methods we compare against. As explained in Sec. VI-C, ground truth phantoms have the different image size of 512×512, so we downscale those phantoms by half, and then compute PSNR and SSIM between the downscaled phantoms

TABLE I
MEAN AND STANDARD DEVIATION OF PSNR AND SSIM WITH VARYING NOISE LEVELS η

η	PSNR			SSIM		
	SART	TVR-D	DALM	SART	TVR-D	DALM
0.00	24.5±4	24.2±4	24.8±4	0.88±0.08	0.96±0.02	0.97±0.01
0.01	23.8±4	22.7±3	24.7±3	0.84±0.10	0.93±0.05	0.97±0.01
0.02	22.4±4	19.4±8	24.1±3	0.76±0.12	0.82±0.15	0.96±0.02
0.03	20.8±5	19.0±7	23.1±4	0.70±0.13	0.81±0.16	0.90±0.11

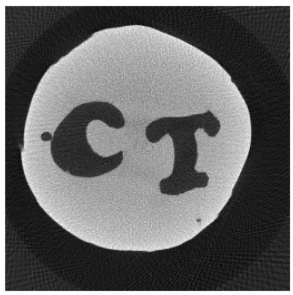

Fig. 14. Reference reconstruction image by filtered backprojection from the carved cheese data with 180 projection angles.

and the solutions. In Table I we provide the quantitative results by PSNR and SSIM with different noise levels. Our result is shown to give better results in all noise levels. In this result we use 5 phantoms and present the mean and standard deviation values.

The large standard deviation for the three methods might indicate that the difference between the means is not significant. Therefore, we performed a three-way ANOVA with no interaction between variables. The results for both PSNR and SSIM show that the phantom and the noise level have a very large influence on quality measure, and our method has a smaller, but also significant influence. In conclusion, ANOVA confirms that the quality means for the three methods are significantly different.

E. Effects of Algorithm Parameters

We investigate the main parameters of our method: the initial reconstruction regularization parameter α, the average edge length of the mesh l_1 and the curve regularization parameter λ. We use the same dataset and settings as in Section VI-C. Note that we have two parameters to control the fineness of mesh: the initial edge length l_0 and the average edge length l_1 during

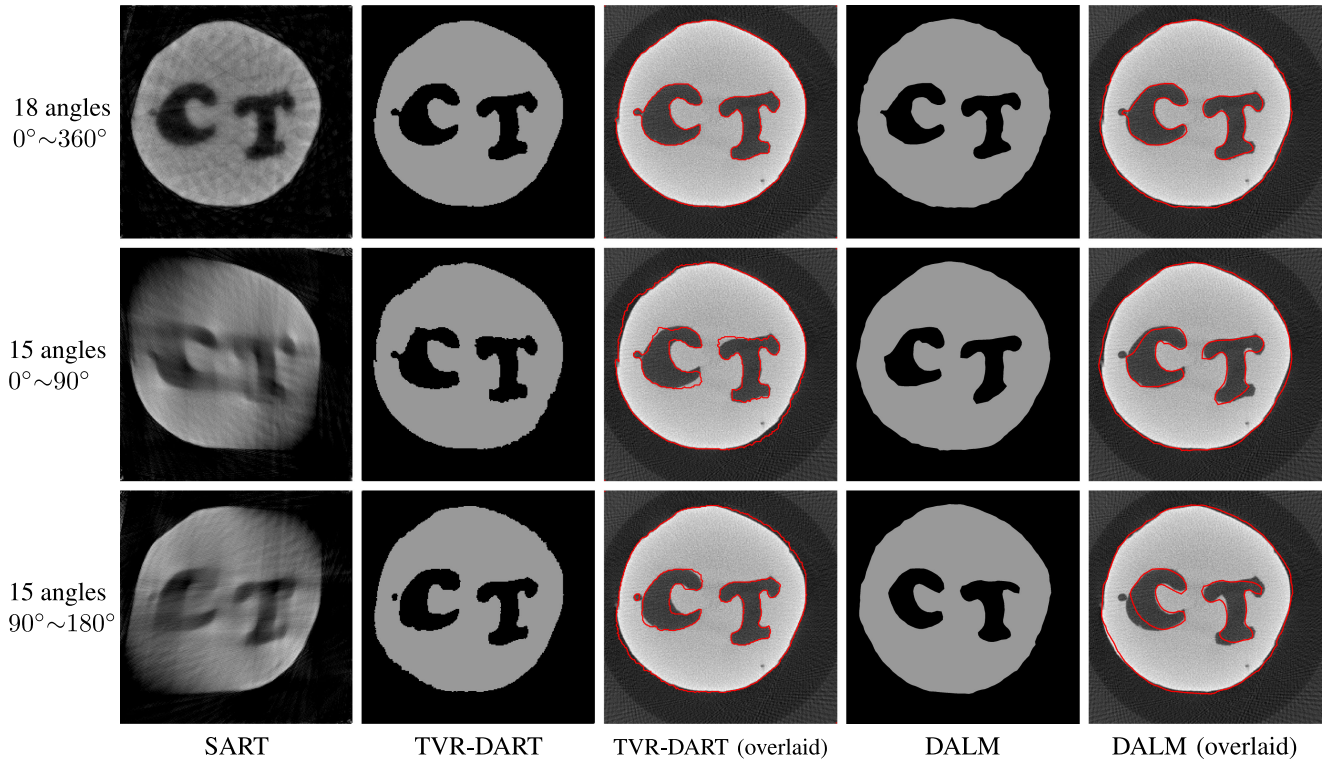

Fig. 15. Reconstruction and segmentation results on real fan-beam data.

TABLE II
COMPUTATIONAL COST AND COMPACTNESS OF MESH WITH WITH VARYING AVERAGE EDGE LENGTH l_1

avg. edge length (pixel)	4	6	8	10
# of vertices	6616	1278	815	723
# of edges	19565	3551	2162	1886
# of faces	12950	2274	1348	1164
# of interface vertices	685	469	264	248
initialization (sec)	12.7	12.7	12.7	12.7
compute $\hat{p}$, μ & disp.	10.3	8.5	5.1	4.6
deformation	77.1	41.0	24.8	20.4
total time	100.1	61.2	42.6	37.7

evolution. Throughout the experiment, we fix l_0 as 4 and this parameter affects the initial reconstruction quality and speed. It is desired to choose this parameter as small as possible to capture the details of objects. After initialization, we collapse non-interface edges for computational efficiency, but interface edges are unchanged. This way, we preserve the details on the interface, while non-interface regions have a more coarse mesh. Subsequently, the average edge length l_1 controls the fineness of the mesh during evolution.

In Fig. 13, segmentation results of Phantom 3 are provided with varying average edge length l_1. As l_1 increases, we have the compact representation of objects, while preserving the outlines of objects. In Table II, we provide the information of final mesh and computational cost with different average edge length. As expected, as average edge length is higher, we obtain more compact representation of objects and reduce the computational cost. To investigate the cost of each step, we divide the total time into three steps: first, initialization; second, computing forward projections, attenuation coefficients and displacements; third, the deformation step. Most of the computational cost is attributed to the deformation part. Based on this, we identify the mesh deformation model as the critical step. A more efficient deformation model could therefore be a candidate for improving the algorithm speed. For other image-based methods, the computational time is 13.6 seconds for SART and 42.4 seconds for TVR-DART. Both methods reconstruct 65 536 pixels. For the experiments, we use a laptop with 3.5 GHz processor and 16 GB memory.

The initial regularization parameter α controls the smoothness of the initial reconstruction result. We observe that our method is not sensitive to initialization in the simple datasets such as Phantom 1, 2, 3 and 4, but sensitive in Phantom 5. We leave as a future work to solve the apparent issue of initialization.

In Fig. 12, we provide the effects of the main parameters with different noise levels. For this experiment, we use Phantom 1 and show how residual reprojection errors are affected. In (a) we show the effect of fineness of mesh. We set both the initial edge length l_0 and the average edge length l_1 as the same values, so that the fineness of mesh is fixed from initialization to the end. As those values increase, overall, the residual projection error also increases. So there is a trade-off between accuracy and compactness of representation. In (b) it is shown that as the relative noise level increases, so does the optimal parameter of curve regularization λ. If the data is noisy or incomplete, we need stronger regularization. Note that, in addition, the deformation step has a regularization effect intrinsic to DSC. In (c) we see that the initialization smoothness parameter α does not affect the error, significantly.

F. Real Dataset

In the following, we perform an experiment on real fan-beam data provided by [39]. The authors of [39] carved out the letters

'CT' in a cheese. The carved cheese was scanned using micro-CT under the exposure time of 1000 ms, the acceleration voltage of 40 kV and the current of 1 mA in X-ray tube [39]. Two phases (materials) are present: cheese and air. The geometry of the scanning is flat fan-beam, and the number of detector pixels is 989. For this data we do not have the exact ground truth, but we consider the reconstruction by FBP from sinogram with 180 angles as the reference image shown in Fig. 14.

We compare our methods in challenging cases under the small number of projection angles or limited range of angles. In Fig. 15, we provide the reconstruction and segmentation results from SART, TVR-DART and our method, DALM. The first row shows the results when using sinogram from 18 projection angles. The second and third row present the results from limited angle data with 15 angles of 0–90 ° and 90–180 °, respectively. As TVR-DART and our method give the segmentation results, we provide the estimated boundaries overlaid on the reference image on the third and last column, respectively. DALM captures the shape of the object, even in the limited angle data. Overall, our method is shown to give slightly smaller letters due to regularization of curves.

VII. Conclusion and Discussion

We have presented DALM, a mesh-based method for 2D reconstruction and segmentation directly from sinogram data. In DALM, a labeled mesh is deformed to align interface edges with object boundaries. By using mesh deformation which supports topological changes and prevents self-intersections, DALM overcomes the drawbacks of existing explicit representation-based methods [2], [27], [40]. Moreover, our method easily supports multiple objects, while in popular level-set methods, supporting multiple regions is not straightforward and additional efforts are required [41]. Experimental results on synthetic data show that our method gives an accurate geometric solution with a compact representation of objects. We provide an efficient forward projection scheme, while the deformation step costs more in terms of computation time. We leave for future work to speed up the deformation step and extend to 3D reconstruction.

Appendix
Derivation of the Curve Evolution Equation (4)

To derive the evolution equation (4), we begin with the case of single material. Let C_m denote the curve to represent the boundary of foreground object with material μ_m and the air background. We introduce an artificial time parameter t and assume that the detector positions s are sampled dense enough. Following [16], the curve evolution equation for C_m is

$$\frac{\partial C_m(r)}{\partial t} = \left(\mu_m \sum_{\theta} (p(\theta, \tilde{s}) - \hat{p}(\theta, \tilde{s})) + \bar{\lambda} \kappa_m(r) \right) N_m(r), \tag{20}$$

where κ_m is the curvature, N_m is the outward normal vector, $\tilde{s} = L_\theta(C_m(r))$ with r the arc length parameter and $\bar{\lambda}$ is the regularization parameter.

We now extend to M multiple materials where the domain is divided by mutually disjoint regions $\{R_m\}$ and the curves $\{C_m\}$ represent their boundaries. Let the region R_m be adjacent to the region R_n with the boundary C_n and the attenuation μ_n. Then, for the points on $C_m \cap C_n \neq \emptyset$, the curve evolution equation for C_m is given [27]:

$$\begin{aligned} \frac{\partial C_m(r)}{\partial t} = & \left(\mu_m \sum_{\theta} (p(\theta, \tilde{s}) - \hat{p}(\theta, \tilde{s})) + \bar{\lambda} \kappa_m(r) \right) N_m(r) \\ & + \left(\mu_n \sum_{\theta} (p(\theta, \tilde{s}) - \hat{p}(\theta, \tilde{s})) + \bar{\lambda} \kappa_n(r) \right) N_n(r). \end{aligned} \tag{21}$$

For the points on $C_m \cap C_n$, the normal vectors and the curvatures have the opposite sign such that $N_m = -N_n$ and $\kappa_m = -\kappa_n$ [27]. Plugging these relations into (21), we have

$$\begin{aligned} \frac{\partial C_m(r)}{\partial t} = & \left((\mu_m - \mu_n) \sum_{\theta} (p(\theta, \tilde{s}) - \hat{p}(\theta, \tilde{s})) + 2\bar{\lambda} \kappa_m(r) \right) \\ & \times N_m(r). \end{aligned} \tag{22}$$

From this equation, we derive (4) with the fixed step size τ and $\lambda := 2\bar{\lambda}$.

Acknowledgment

The authors thank Patrick M. Jensen for the fruitful discussion and proofreading the paper.

References

[1] G. T. Herman, *Fundamentals of Computerized Tomography: Image Reconstruction from Projections*, 2nd ed., *Ser. Advances in Pattern Recognit.*, Dordrecht, The Netherlands; New York, NY, USA: Springer, 2009.

[2] V. A. Dahl, A. B. Dahl, and P. C. Hansen, "Computing segmentations directly from x-ray projection data via parametric deformable curves," *Meas. Sci. Technol.*, vol. 29, no. 1, 2018, Art. no. 014003.

[3] M. K. Misztal and J. A. Bærentzen, "Topology-adaptive interface tracking using the deformable simplicial complex," *ACM Trans. Graph.*, vol. 31, no. 3, pp. 1–12, 2012.

[4] K. J. Batenburg and J. Sijbers, "DART: A practical reconstruction algorithm for discrete tomography," *IEEE Trans. Image Process.*, vol. 20, no. 9, pp. 2542–2553, Sep. 2011.

[5] K. J. Batenburg, W. van Aarle, and J. Sijbers, "A semi-automatic algorithm for grey level estimation in tomography," *Pattern Recognit. Lett.*, vol. 32, no. 9, pp. 1395–1405, 2011.

[6] F. Bleichrodt, F. Tabak, and K. J. Batenburg, "SDART: An algorithm for discrete tomography from noisy projections," *Comput. Vis. Image Underst.*, vol. 129, pp. 63–74, 2014.

[7] X. Zhuge, W. J. Palenstijn, and K. J. Batenburg, "TVR-DART: A more robust algorithm for discrete tomography from limited projection data with automated gray value estimation," *IEEE Trans. Image Process.*, vol. 25, no. 1, pp. 455–468, Jan. 2016.

[8] A. Tuysuzoglu, Y. Khoo, and W. C. Karl, "Variable splitting techniques for discrete tomography," in *Proc. IEEE Int. Conf. Image Process.*, 2016, pp. 1764–1768.

[9] F. Lauze, Y. Quéau, and E. Plenge, "Simultaneous reconstruction and segmentation of CT scans with shadowed data," in *Scale Space and Variational Methods in Computer Vision*, F. Lauze, Y. Dong, and A. Dahl, Eds., vol. 10302. Cham, Switzerland: Springer, 2017.

[10] A. Tuysuzoglu, W. C. Karl, I. Stojanovic, D. Castañòn, and M. S. Ünlü, "Graph-cut based discrete-valued image reconstruction," *IEEE Trans. Image Process.*, vol. 24, no. 5, pp. 1614–1627, May 2015.

[11] J. H. Kappes, S. Petra, C. Schnörr, and M. Zisler, "TomoGC: Binary tomography by constrained graphcuts," in *German Conference on Pattern Recognition*, J. Gall, P. Gehler, and B. Leibe, Eds., Berlin, Germany: Springer, 2015, pp. 262–273.

[12] Z. Wei, B. Liu, B. Dong, and L. Wei, "A joint reconstruction and segmentation method for limited-angle X-ray tomography," *IEEE Access*, vol. 6, pp. 7780–7791, 2018.

[13] S. Osher and J. A. Sethian, "Fronts propagating with curvature-dependent speed: Algorithms based on Hamilton-Jacobi formulations," *J. Comput. Phys.*, vol. 79, no. 1, pp. 12–49, 1988.

[14] R. T. Whitaker and V. Elangovan, "A direct approach to estimating surfaces in tomographic data," *Med. Image Anal.*, vol. 6, no. 3, pp. 235–249, 2002.
[15] D. Mumford and J. Shah, "Optimal approximations by piecewise smooth functions and associated variational problems," *Commun. Pure Appl. Math.*, vol. 42, no. 5, pp. 577–685, 1989.
[16] C. V. Alvino and A. J. Yezzi, "Tomographic reconstruction of piecewise smooth images," in *Proc. IEEE Conf. Comput. Vis. Pattern Recognit.*, 2004.
[17] S. Yoon, A. R. Pineda, and R. Fahrig, "Simultaneous segmentation and reconstruction: A level set method approach for limited view computed tomography," *Med. Phys.*, vol. 37, no. 5, pp. 2390–2340, 2010.
[18] R. Ramlau and W. Ring, "A mumford level-set approach for the inversion and segmentation of X-ray tomography data," *J. Comput. Phys.*, vol. 221, no. 2, pp. 137–166, 2007.
[19] A. Aghasi, M. Kilmer, and E. L. Miller, "Parametric level set methods for inverse problems," *SIAM J. Imag. Sci.*, vol. 4, no. 2, pp. 618–650, 2011.
[20] A. Kadu, T. van Leeuwen, and K. J. Batenburg, "A parametric level-set method for partially discrete tomography," in *Proc. Int. Conf. Discrete Geometry Comput. Imagery*, 2018.
[21] J. G. Brankov, Y. Yang, and M. N. Wernick, "Tomographic image reconstruction based on a content-adaptive mesh model," *IEEE Trans. Med. Imag.*, vol. 23, no. 2, pp. 202–212, Feb. 2004.
[22] A. Cazasnoves, F. Buyens, and S. Sevestre-Ghalila, "Adapted sampling for 3D X-ray computed tomography," in *Proc. 13th Int. Meeting Fully Three-Dimensional Image Reconstruction Radiol. Nucl. Med.*, 2015.
[23] A. Sitek, R. Huesman, and G. Gullberg, "Tomographic reconstruction using an adaptive tetrahedral mesh defined by a point cloud," *IEEE Trans. Med. Imag.*, vol. 25, no. 9, pp. 1172–1179, Sep. 2006.
[24] N. F. Pereira and A. Sitek, "Evaluation of a 3D point cloud tetrahedral tomographic reconstruction method," *Phys. Med. Biol.*, vol. 55, no. 18, pp. 5341–5361, 2010.
[25] R. Boutchko, A. Sitek, and G. T. Gullberg, "Practical implementation of tetrahedral mesh reconstruction in emission tomography," *Phys. Med. Biol.*, vol. 58, no. 9, pp. 3001–3022, 2013.
[26] F. Buyens, M. Quinto, and D. Houzet, "Adaptive mesh reconstruction in X-ray tomography," in *Proc. MICCAI Workshop Mesh Process. Med. Image Anal.*, 2013.
[27] S. C. Zhu, T. S. Lee, and A. L. Yuille, "Region competition: Unifying snakes, region growing, energy/bayes/MDL for multi-band image segmentation," in *Proc. IEEE Int. Conf. Comput. Vis.*, 1995, pp. 416–423.
[28] B. O'Neill, *Elementary Differential Geometry*. Amsterdam; Boston: Elsevier Academic Press, 2006.
[29] G. Strang, *Linear Algebra and Its Applications*, 4th ed. Belmont, CA: Thomson, Brooks/Cole, 2006.
[30] S. P. Lloyd, "Least squares quantization in PCM," *IEEE Trans. Inf. Theory*, vol. 28, no. 2, pp. 129–137, Mar. 1982.
[31] T. M. Buzug, *Computed Tomography From Photon Statistics to Modern Cone Beam CT*. Berlin, Germany: Springer, 2008.
[32] F. Mahmood, N. Shahid, U. Skoglund, and P. Vandergheynst, "Adaptive graph-based total variation for tomographic reconstructions," *IEEE Signal Process. Lett.*, vol. 25, no. 5, pp. 700–704, May 2018.
[33] A. Chambolle and T. Pock, "A first-order primal-dual algorithm for convex problems with applications to imaging," *J. Math. Imag. Vis.*, vol. 40, no. 1, pp. 120–145, 2011.
[34] E. Y. Sidky, J. H. Jørgensen, and X. Pan, "Convex optimization problem prototyping for image reconstruction in computed tomography with the chambolle-pock algorithm," *Phys. Med. Biol.*, vol. 57, no. 10, pp. 3065–3091, 2012.
[35] D. J. Ching and D. Gürsoy, "XDesign : An open-source software package for designing X-ray imaging phantoms and experiments," *J. Synchrotron Radiat.*, vol. 24, no. 2, pp. 537–544, 2017.
[36] W. van Aarle *et al.*, "Fast and flexible X-ray tomography using the ASTRA toolbox," *Opt. Exp.*, vol. 24, no. 22, pp. 25129–25147, 2016.
[37] A. H. Andersen and A. C. Kak, "Simultaneous algebraic reconstruction technique (SART): A superior implementation of the ART algorithm," *Ultrason. Imag.*, vol. 6, no. 1, pp. 81–94, 1984.
[38] T. Roelandts, K. J. Batenburg, A. J. den Dekker, and J. Sijbers, "The reconstructed residual error: A novel segmentation evaluation measure for reconstructed images in tomography," *Comput. Vis. Image Underst.*, vol. 126, pp. 28–37, 2014.
[39] T. A. Bubba *et al.*, "Tomographic X-ray data of carved cheese," *Med. Phys.*, 2017 *arXiv:170505732*.
[40] M. Kass, A. Witkin, and D. Terzopoulos, "Snakes: Active contour models," *Int. J. Comput. Vis.*, vol. 1, no. 4, pp. 321–331, 1988.
[41] L. A. Vese and T. F. Chan, "A multiphase level set framework for image segmentation using the mumford and shah model," *Int. J. Comput. Vis.*, vol. 50, no. 3, pp. 271–293, 2002.

Jakeoung Koo received the B.Sc. and M.Eng. degrees from Chung-Ang University, South Korea, in 2015 and 2017, respectively. He is currently working toward the Ph.D. degree with the Department of Applied Mathematics and Computer Science, Technical University of Denmark (DTU). His research interests include computational imaging and computer vision. His current work is on tomographic reconstruction where he investigates alternative representations such as meshes, instead of discrete images.

Anders Bjorholm Dahl is a Professor in 3D image analysis, and a Head of the Section for Image Analysis and Computer Graphics with DTU Compute, Technical University of Denmark (DTU). He is heading The Center for Quantification of Imaging Data from MAX IV, which focuses on research in quantitative analysis of 3D microscopy images. This is done through research collaboration with scientists using 3D imaging, development of software tools, and research in 3D image analysis tools.

Vedrana Andersen Dahl holds degrees in mathematics, multimedia technology, and the Ph.D. degree in geometry processing. She is an Associate Professor with the Department of Applied Mathematics and Computer Science, Technical University of Denmark. Her primary research interest focuses on using geometric models for the analysis of volumetric data. This includes volumetric segmentation, tomographic segmentation, and methods based on deformable meshes. She developed analysis tools with applications in material science, industrial inspection, and biomedicine.